

Review

Investigating the Properties of the Relativistic Jet and Hot Corona in AGN with X-ray Polarimetry

Dawoon E. Kim^{1,2,3,*}, Laura Di Gesu⁴, Frédéric Marin⁵, Alan P. Marscher⁶, Giorgio Matt⁷, Paolo Soffitta¹, Francesco Tombesi^{3,8,9}, Enrico Costa¹ and Immacolata Donnarumma⁴

- ¹ INAF Istituto di Astrofisica e Planetologia Spaziali, Via del Fosso del Cavaliere 100, 00133 Roma, Italy; paolo.soffitta@iaps.inaf.it (P.S.); enrico.costa@iaps.inaf.it (E.C.)
 - ² Dipartimento di Fisica, Università degli Studi di Roma “La Sapienza”, Piazzale Aldo Moro 5, 00185 Roma, Italy
 - ³ Dipartimento di Fisica, Università degli Studi di Roma “Tor Vergata”, Via della Ricerca Scientifica 1, 00133 Roma, Italy; francesco.tombesi@roma2.infn.it (F.T.)
 - ⁴ ASI-Agenzia Spaziale Italiana, Via del Politecnico snc, 00133 Roma, Italy; laura.digesu@asi.it (L.D.G.); immacolata.donnarumma@asi.it (I.D.)
 - ⁵ Université de Strasbourg, CNRS, Observatoire Astronomique de Strasbourg, UMR 7550, 67000 Strasbourg, France; frederic.marin@astro.unistra.fr (F.M.)
 - ⁶ Institute for Astrophysical Research, Boston University, 725 Commonwealth Avenue, Boston, MA 02215, USA; marscher@bu.edu (A.P.M.)
 - ⁷ Dipartimento di Matematica e Fisica, Università degli Studi Roma Tre, Via della Vasca Navale 84, 00146 Roma, Italy; giorgio.matt@uniroma3.it (G.M.)
 - ⁸ Istituto Nazionale di Fisica Nucleare, Sezione di Roma “Tor Vergata”, Via della Ricerca Scientifica 1, 00133 Roma, Italy
 - ⁹ Department of Astronomy, University of Maryland, College Park, MD 20742, USA
- * Correspondence: dawoon.kim@inaf.it

Abstract: X-ray polarimetry has been suggested as a prominent tool for investigating the geometrical and physical properties of the emissions from active galactic nuclei (AGN). The successful launch of the Imaging X-ray Polarimetry Explorer (IXPE) on 9 December 2021 has expanded the previously restricted scope of polarimetry into the X-ray domain, enabling X-ray polarimetric studies of AGN. Over a span of two years, IXPE has observed various AGN populations, including blazars and radio-quiet AGN. In this paper, we summarize the remarkable discoveries achieved thanks to the opening of the new window of X-ray polarimetry of AGN through IXPE observations. We will delve into two primary areas of interest: first, the magnetic field geometry and particle acceleration mechanisms in the jets of radio-loud AGN, such as blazars, where the relativistic acceleration process dominates the spectral energy distribution; and second, the geometry of the hot corona in radio-quiet AGN. Thus far, the IXPE results from blazars favor the energy-stratified shock acceleration model, and they provide evidence of helical magnetic fields inside the jet. Concerning the corona geometry, the IXPE results are consistent with a disk-originated slab-like or wedge-like shape, as could result from Comptonization around the accretion disk.

Keywords: X-ray polarimetry; active galactic nuclei; relativistic jets

1. Introduction

Active galactic nuclei (AGN) stand out as fascinating and powerful sources (with bolometric luminosities $\sim 10^{42}$ – 10^{46} erg s⁻¹; e.g., [1,2]) that emit electromagnetic radiation across the entire spectrum, ranging from radio wavelengths to gamma rays. Specifically, in the X-ray regime, emissions originate from the vicinity of the central engine, in either the inner part of the jet or in an X-ray corona. The high penetration power of X-ray radiation facilitates the unobstructed study of processes near black holes. So far, X-ray probes have been limited to spectral and timing techniques [3]. Although these methods provide

arXiv:2404.14200v1 [astro-ph.HE] 22 Apr 2024



Citation: Kim, D.E.; Di Gesu, L.; Marin, F.; Marscher, A.P.; Matt, G.; Soffitta, P.; Tombesi, F.; Costa, E.; Donnarumma, I. Investigating the Properties of the Relativistic Jet and Hot Corona in Agn with X-ray Polarimetry. *Galaxies* **2024**, *1*, 0. <https://doi.org/>

Academic Editor: Ilaria Ruffa

Received: 29 February 2024

Revised: 5 April 2024

Accepted: 12 April 2024

Published:



Copyright: © 2024 by the authors. Licensee MDPI, Basel, Switzerland. This article is an open access article distributed under the terms and conditions of the Creative Commons Attribution (CC BY) license (<https://creativecommons.org/licenses/by/4.0/>).

clues about the radiative processes producing X-rays in the inner AGN region, they are insensitive to some key characteristics, such as the geometry of the emitting region or the magnetic field, which so far have remained largely unconstrained.

In this context, polarimetric studies have been suggested as a prominent tool for investigating the geometrical and physical properties of AGN emissions [4]. The successful launch of the Imaging X-ray Polarimetry Explorer (IXPE) on 9 December 2021 marked a significant advancement in polarimetry by extending it into the X-ray range [5]. IXPE is a collaborative mission between NASA and the Italian Space Agency (Agenzia Spaziale Italiana, ASI). It comprises three identical X-ray telescope systems, each one composed of one mirror module assembly and one detector unit hosting a gas pixel detector [6] with a full calibration and filtering system. IXPE is designed to measure the linear polarization in the 2–8 keV band using polarization mapping techniques. It offers a field of view greater than $11'$ and an angular resolution of less than or equal to $30''$. Over the first two years of operation, IXPE has detected X-ray polarization from several AGN, helping to address the long-standing uncertainty about the jet magnetic field structure and acceleration process and the geometry of the X-ray corona.

Traditionally, AGN are divided into two main classes: radio-loud (RLAGN) and radio-quiet (RQAGN), based on their radio to optical flux ratio [7,8]. In some cases, they are classified as jetted or non-jetted based on the presence or absence of strong relativistic jets [9]. Among the population of RLAGN, blazars are ideal targets for studying relativistic jets because, in these sources, the jet flow is relatively closely aligned to the observer's line of sight, and their emission is dominated by jet emission across the entire spectral energy distribution (SED) due to relativistic Doppler boosting, e.g., [10]. The SED of blazars exhibits two broad non-thermal radiation components as shown in Figure 1. One component, located in the lower-frequency range, covers emissions from radio to optical/UV (and, in some cases, to X-ray) and is generally ascribed to synchrotron emission from relativistic electrons. The other component may be explained in two different scenarios: leptonic or hadronic models. In the leptonic process, the high-energy emission is attributed to Compton scattering of synchrotron photons (synchrotron self-Compton or SSC; e.g., [11,12]) or photons originating outside the jet (external Compton or EC; e.g., [13–15]). In the hadronic scenario, proton synchrotron emission, π_0 decay photons, synchrotron, and Compton emission from secondary decay products of charged pions have been suggested, e.g., [16–18]. These emission processes are predicted to produce different X-ray polarization properties depending on the acceleration mechanism in both leptonic and hadronic scenarios [19]. Furthermore, depending on the position of the peak frequency of the electron synchrotron emission hump (ν_{peak}), blazars are separated into low- ($\nu_{peak} < 10^{14}$ Hz or $3 \mu\text{m}$; LSP), intermediate- ($\nu_{peak} \sim 10^{14}$ Hz– 10^{15} Hz; ISP), and high-synchrotron-peak ($\nu_{peak} > 10^{15}$ Hz or $0.3 \mu\text{m}$; HSP) subclasses [20]. Therefore, studying various subclasses of blazars with X-ray polarimetry allows us to explore different physical processes. First, with HSP targets, the particle acceleration process and geometrical features of the magnetic field inside the jets can be studied. Second, with ISP and LSP blazars, the superposition of synchrotron emission and leptonic or hadronic emission in spectra enables tests of the acceleration mechanisms behind the high-energy emission hump.

In the case of RQAGN, given that they are not typically dominated by jet emissions, we can observe other emission components surrounding the central engine (see Figure 1). The primary X-ray emission of AGN is believed to originate from a corona of hot (with a temperature of 10–100 keV) and optically thin (or mildly thick) plasma that Compton scatters the optical/UV photons from the accretion disk, e.g., [21]. Additionally, these X-ray photons are reflected (backscattered) either by the accretion disk or by the more distant torus, which results in additional X-ray spectral components as secondary emissions [22]. RQAGN are divided into Seyfert 1 and 2 galaxies based on whether or not both broad and narrow emission lines are observed in the optical band, which partially depends on the differences in the line of sight direction [23]. In the X-ray regime, Seyfert 1 galaxies, which have a relatively small inclination angle between our line of sight and the axis of the

system, averaging 39° [24,25], show unobscured X-ray coronae and disk reflection, while the emission from Seyfert 2s is dominated by photons reprocessed through reflection from the strongly absorbing dusty torus and from the polar winds due to the larger inclination angle.

The spectrum of the corona typically follows a power law with a high-energy cutoff, e.g., [26]. The slope of the power law is determined by the electron temperature and the optical depth, while the cutoff energy depends mostly on the electron temperature. The size and geometry of the corona remain elusive, although these characteristics are crucial for differentiating between models for the formation of AGN coronae, e.g., [27]. Regarding the geometric characteristics of the hot corona, several possibilities have been suggested, including lamppost, spherical, conical, slab, and wedge. In particular, spherical or conical structures located on the rotation axis above and below the black hole would suggest a potential connection between the corona and the jet, e.g., [28,29]. In this context, it is predicted that the X-ray polarization of the corona emission depends on the geometry, e.g., [30], and demonstrates that X-ray polarization measurements can serve as a powerful tool for probing the disk/corona geometry, e.g., [31,32]. Hence, the polarization observations of unobscured RQAGN can provide valuable insights into the geometric features of the corona.

In this short review, we will briefly summarize the theoretical expectations and remarkable discoveries obtained from the first two years of IXPE observations of RLAGN and RQAGN. These concern the magnetic field geometry and particle acceleration mechanisms in the jets, as well as the geometry of the hot corona. We will then discuss future prospects.

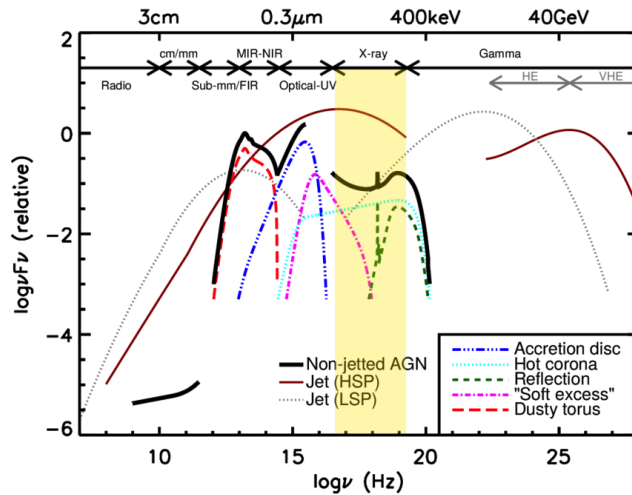


Figure 1. A schematic representation of SED for RLAGN (HSP: red solid line, and LSP: gray dotted line) and RQAGN (black solid line with labeled colored lines for different emission components). The yellow shaded area indicates the X-ray regime. The figure is reproduced from Figure 1 in [8].

2. X-ray Polarization from Relativistic Jets

2.1. Theoretical Expectations

The observed emission coming from relativistic jets is often well-described by a power law spectrum within a given frequency band. Theoretically, this can be explained as synchrotron radiation produced by a power law energy spectrum of electrons with Lorentz factor γ , $N_e(\gamma) \propto \gamma^{-p}$, which produces a power law synchrotron radiation spectrum $F_\nu \propto \nu^{-\alpha}$, with $\alpha = (p - 1)/2$. This results in a polarization degree (Π) of [4]

$$\Pi_{\text{sync}} = \frac{p + 1}{p + 7/3} = \frac{\alpha + 1}{\alpha + 5/3}. \quad (1)$$

Considering the typical power law index obtained from blazars $\sim p = 2-3$, a polarization degree of the electron synchrotron emission in a homogeneous magnetic field is expected to be $\Pi \sim 70\%$. The polarization angle (ψ) is perpendicular to the averaged mag-

netic field direction projected onto the sky plane. However, in reality, polarization can be reduced by the geometrical and physical properties within the jet, such as temporal variation effects occurring over timescales shorter than the integration time of the polarization measurement [33–35]. Thereby, in order to explain the polarization measurements and variability, various geometrical and physical models have been suggested. For instance, for the geometrical model, there have been several suggestions: a bending jet [36], a spiral motion model in which a blob propagates in a spiral trajectory within a helical magnetic field [37], and the ballistic motion of an emission blob in a jet with a helical magnetic field [38]. In the case of the physical conditions, there have been several suggestions as well: many turbulent cells, the TEMZ model, [39–41], shock and kink instabilities that can efficiently dissipate jet bulk energy to accelerate particles [42–45], and magnetic reconnection [46–49]. Refs. [50,51] have presented the predicted X-ray and simultaneous multiwavelength polarization characteristics among various theoretical models as follows: (1) in the shock acceleration model, particle acceleration is characterized by a strong self-generated magnetic field. Hence, a large degree of polarization, $\Pi_X \sim 40\%$, and relatively stable Π_X and ψ_X over time (variability in a few days to a week) are predicted [52,53]. Moreover, a chromatic feature in X-ray and optical polarization, where $\Pi_X/\Pi_O \gtrsim 2$, is anticipated because particles emitting at longer wavelengths, due to their longer synchrotron cooling time, travel away from the shock front to regions with a more disordered magnetic field; (2) in the magnetic reconnection model, the reconnection episodes are triggered by instability induced, for example, by current sheets [46,54]. $\Pi_X \lesssim 20 - 30\%$ and similar characteristics for Π_O are predicted as a result of the simultaneous contribution of several active current sheets with different orientations. Additionally, the evolution of the instability results in significant variations, and ψ_X can show variability on a daily timescale; (3) in the TEMZ model, $\Pi_X \lesssim 30\%$ and rapid changes in Π_X and ψ_X less than a day timescale are predicted because of the superposition of the emission of several cells, in which the magnetic field is uniform but randomly oriented [39]. In addition, mild chromatic behavior, $\Pi_X/\Pi_O \lesssim 2$, is expected as a large number of cells can radiate at lower frequencies. Thus, the variability is erratic and somewhat driven by the dimension and number of cells. Consequently, expanding multiwavelength polarimetric measurements on synchrotron emission to the X-ray band provides clues about the layout of the magnetic field as particles emitting at different energies can assist in identifying the predominant acceleration process.

Compton scattering of unpolarized seed photons by highly relativistic electrons produces zero polarization in the scattered radiation [55]. Therefore, detecting X-ray polarization from LSP blazars, whose emission component is primarily dominated by Compton scattering in X-rays, would effectively rule out the possibility of EC processes. In contrast, under the conditions of proton synchrotron radiation, the polarization levels could potentially reach around 70%, consistent with the proton spectral indices in Equation (1), where p is approximately 2–3 [55]. A polarization degree significantly higher than that at mm-waves and similar to or greater than that at optical wavelengths, and a slope of the X-ray emission that is sufficiently flat, could be interpreted as an indication of proton synchrotron emission. Furthermore, for cases involving a combination of synchrotron emission at soft X-ray energies and SSC/EC at harder X-rays, detailed SED modeling and decomposition of the polarization properties of each component are required. The model considering multiple emission zones with turbulent magnetic fields predicts $\Pi_{SSC}/\Pi_{Sync} \approx 0.3$ [56].

2.2. IXPE Observations of High Synchrotron Peak Blazars

IXPE observations of HSP blazars have been conducted for Mrk 501 [57], Mrk 421 [58–60], 1ES1959+650 [61], PG1553+113 [62], and 1ES0229+200 [63]. The X-ray polarization of each target was estimated through time-averaged analysis by considering the entire observation period and time- and energy-resolved analyses by dividing the observations into sub-segments using model independent event Stokes parameter analysis [64] and spectropolarimetric analysis [65]. In addition, during all the IXPE blazar observations, a simultaneous multiwavelength polarimetry campaign was conducted, including

radio, infrared (IR), and optical wavelengths, to examine the synchrotron emission properties across different wavelengths. In this section, we summarize the reported X-ray and multiwavelength polarimetry features of each observation, as well as the X-ray spectral properties. Table 1 presents a summary of the time-averaged multiwavelength polarization information for all the HSP observations, and Table 2 provides a summary of the X-ray spectral characteristics, including the photon index and flux derived based on the log parabolic model [66]. The log parabolic model represents power laws with a photon index that varies according to a log parabola in energy:

$$N(E) = K(E/E_{pivot})^{(\alpha - \beta \log(E/E_{pivot}))}, \quad (2)$$

where the pivot energy E_{pivot} is a scaling factor, α describes the slope of the photon spectrum at E_{pivot} , β expresses the spectral curvature, and K denotes a normalization constant.

Table 1. Contemporaneous multiwavelength polarization properties of HSPs.

Source	X-ray		Optical & IR ^a		Radio ^a	
	Π (%)	ψ (°)	Π (%)	ψ (°)	Π (%)	ψ (°)
Mrk 501 I ¹	10 ± 2	134 ± 5	4 ± 1	119 ± 9	1.5 ± 0.5	152 ± 10
Mrk 501 II ¹	11 ± 2	115 ± 4	5 ± 1	117 ± 3	–	–
Mrk 421 I ²	15 ± 2	35 ± 4	2.9 ± 0.5	32 ± 5	3.4 ± 0.4	55 ± 2
Mrk 421 II ³	10 ± 1	Rotation	4.4 ± 0.4	140 ± 6	2.4 ± 0.1	139 ± 8
Mrk 421 III ³	10 ± 1	Rotation	5.4 ± 0.4	145 ± 1	–	–
Mrk 421 IV ⁴	14 ± 1	107 ± 3	4.6 ± 1.3	206 ± 9	1.8 ± 0.1	167 ± 4
1ES1959+650 I ⁵	8 ± 2	123 ± 8	4.5 ± 0.2	159 ± 1	–	–
1ES1959+650 II ⁵	<5	–	4.7 ± 0.6	151 ± 19	<1.6	–
PG1553+113 ⁶	10 ± 2	86 ± 8	4.2 ± 0.5	Rotation	2.6 ± 0.7	133 ± 7
1ES0229+200 ⁷	18 ± 3	25 ± 5	3.2 ± 0.7	−5 ± 9	<7	–

^{1–7} Results compiled from the following references: [57–63]; ^a median polarization properties during the IXPE observation. Especially for optical and IR polarization, only corrected polarization values, accounting for the dilution of polarization by unpolarized starlight from the host galaxy, were considered for calculation; ^b at the lowest radio frequency (4.85 GHz).

Table 2. X-ray spectral properties of HSPs during IXPE observation.

Source	Photon Index	Flux _{2–8 keV} (×10 ^{−11} erg s ^{−1} cm ^{−2})	Telescopes
Mrk 501 I ¹	2.27 ± 0.01	10.0 ± 0.5	IXPE + Swift-XRT+NuSTAR
Mrk 501 II ¹	2.05 ± 0.02	21.0 ± 0.6	IXPE + Swift-XRT
Mrk 421 I ²	2.97 ± 0.01	8.67 ± 0.03	IXPE + XMM-Newton+NuSTAR
Mrk 421 II ³	2.32 ± 0.01 ^a	15.7 ± 0.1	Swift-XRT
Mrk 421 III ³	2.13 ± 0.01 ^a	30.2 ± 0.2	Swift-XRT
Mrk 421 IV ⁴	2.82 ± 0.01	22.5 ± 0.4	IXPE + XMM-Newton
1ES1959+650 I ⁵	2.50 ± 0.02	12.4 ± 0.2	IXPE + XMM-Newton
1ES1959+650 II ⁵	2.29 ± 0.01	14.7 ± 0.1	IXPE + XMM-Newton
PG1553+113 ⁶	2.49 ± 0.01	2.55 ± 0.03	IXPE + XMM-Newton
1ES0229+200 ⁷	1.82 ± 0.01	0.84 ± –	IXPE + XMM-Newton

^{1–7} Results compiled from the following references: [57–63]; ^a average value between variation over time.

Mrk 501 was the first observed HSP blazar. This target was observed at two different epochs (Mrk 501 I: 8–10 March 2022 and Mrk 501 II: 26–28 March 2022). The time-averaged X-ray polarization in the 2–8 keV range of these observations was consistent within a 3σ error range, as shown in Table 1. There was no significant variability within the duration of the individual IXPE observations over time and energy, and the X-ray activity was in an average state. The polarization in the optical, IR, and radio bands was significantly lower than in the X-rays by a factor of ~ 2 , indicating strong chromatic behavior (Figure 2). Additionally, ψ is aligned with the jet direction, $\psi_{43\text{GHz}} = 119.7 \pm 11.8$, obtained from

the 43 GHz Very Long Baseline Array (VLBA) observation [57]. These multiwavelength polarimetric results suggest, among the various proposed models, the “energy-stratified shock acceleration model” in which particles accelerated by shocks experience increasing turbulence as they move away from the accelerating site, resulting in a decrease in the polarization degree. Moreover, shocks can push the particles far away, causing a decrease in Π_X . In addition, the energy-stratified shock acceleration model predicts ψ_X along the jet axis. Thereby, the different polarization angles at different wavelengths suggest a scenario where particles emitting at different energies experience different magnetic field conditions.

Mrk 421 has been observed four times (Mrk 421 I: 4–6 May 2022; Mrk 421 II: 4–6 June 2022; Mrk 421 III: 7–9 June 2022; and Mrk 421 IV: 6–8 December 2022). Mrk 421 I exhibited a slightly higher Π_X of 15% compared to Mrk 501 within a statistical difference of less than 2σ and a Π_X/Π_O ratio of ~ 5 , indicating a stronger chromatic behavior relative to Mrk 501. These results are consistent with the energy-stratified shock acceleration model based on the Π_X/Π_O , where a smaller value was predicted in magnetic reconnection, and the TEMZ models. Subsequent observations of Mrk 421 II and III did not reveal significant polarization information in the time-averaged polarization during the observation periods. However, the time-resolved results, as shown in Figure 2, revealed a smooth rotation of ψ_X by more than 360° between two consecutive observations (Mrk 421 II: from $9 \pm 1^\circ$ to $130 \pm 11^\circ$ and Mrk 421 III: from $222 \pm 7^\circ$ to $360 \pm 20^\circ$). The rotation rates of ψ_X were measured as $80 \pm 9^\circ$ per day and $91 \pm 8^\circ$ per day for the two observations, respectively, while the polarization degrees remained consistent within uncertainty as $\Pi_X = 10 \pm 1\%$. During the observed period, the X-ray flux increased by approximately a factor of two between the two observations and then decreased to a level similar to that at the beginning of the observation, and the spectrum properties showed a decrease in the photon index and an increase in the hardness ratio (i.e., the spectrum became harder and flatter), although we cannot be sure whether this is directly related to the rotation in the polarization angle. The multiwavelength polarimetry results showed chromatic trends consistent with previous findings. Therefore, the results of Mrk 421 II and III suggest a geometric structure where the energy-stratified shock propagates linearly or radially along the helical magnetic field within the jet [59]. Additionally, the Mrk 421 IV showed similar characteristics to those of Mrk 421 I in terms of Π_X , but ψ_X exhibited a different value compared to previous observations (Mrk 421 I, II, and III) and varied across all the observations. In particular, Mrk 421 IV confirmed temporal episodic variability in polarization during this observation period. In particular, Ref. [60] showed a possible correlation between the rotation of ψ_X and the observation of a highly polarized knot emerging from the jet core and moving away from the “core” based on the 43 GHz VLBA observations performed during the observation periods of Mrk 421 II, III, and IV. In addition, multiwavelength polarization monitoring of Mrk 421 I, II, III, and IV showed a rotation of ψ in the optical and radio bands over a longer period compared to the X-ray band, with a direction opposite to the rotation of ψ_X . This result suggests the possibility that emission regions at longer wavelengths (millimeter, infrared, and optical) were separate from, or only partially coincident with, those of the X-ray emission but also contain a helical magnetic field that is presumably a continuation of the helical field manifested in the X-ray polarization observations.

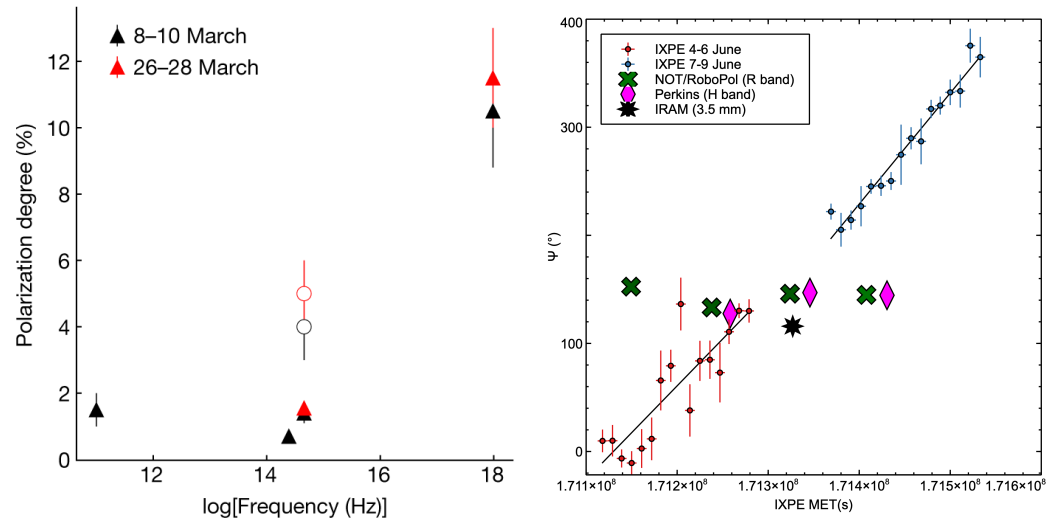


Figure 2. IXPE observation results of Mrk 501 and Mrk 421. **(Left)** Multiwavelength polarization degree of Mrk 501 from radio rays to X-rays. The black symbols represent observations conducted between March 8th and 10th, while the red symbols represent observations from March 26th to 28th. The open symbols indicate the intrinsic optical polarization degree corrected for the host galaxy. The figure was reproduced from Figure 3 in [57]. **(Right)** X-ray polarization angle rotation in Mrk 421. The symbols identify multiwavelength polarimetry measurements obtained from telescopes as labeled. The figure was reproduced from Figure 2 in [59].

In addition, the observations of 1ES1959+650 [61], PG1553+113 [62], and 1ES0229+200 [63] exhibited significant chromatic behavior on Π across multiwavelengths, consistent with the energy-stratified shock acceleration model. Furthermore, concerning energy stratification and cooling inside the shock, the Π_X/Π_O ratio from all the IXPE HSP observations has typically been found to be around ~ 2 – 6 , with a trend between the Π_X/Π_O ratio and Π_X , as shown in the left panel of Figure 3. Consequently, as Π_X/Π_O increases, X-ray emission occurs in smaller volumes due to a relatively shorter cooling timescale, indicating well-ordered magnetic fields closer to the shock front and increased turbulence in the downstream direction [67]. Moreover, the comparison between the Π_X/Π_O ratio and the time-averaged photon index in the right panel of Figure 3 suggests a possibility of relatively higher Π_X/Π_O ratios when the spectrum is softer and steeper, but excluding the observations of 1ES0229+200. Especially in the case of 1ES0229+200, an E_{pivot} scale factor of 1 was used in the log parabolic model instead of the common 5 used in other observations [57,59,60]. Therefore, it is possible that this factor may have influenced the observed results compared to other observations, and this could be improved through analysis under similar conditions in the future. Additionally, this characteristic can be interpreted based on the same physical interpretation as when the X-ray emission originates further away from the peak frequency on the spectrum, indicating that the emission is from well-ordered magnetic fields in a smaller volume with a shorter cooling timescale closer to the shock front.

Regarding the variability in polarization properties, smooth rotation on ψ_X and transient ψ_X variation have been observed only in Mrk 421. Hence, it is speculated that the polarization variability observed exclusively in specific targets may be linked to the inherent physical properties of jets. However, it is imperative to scrutinize statistically significant results through concurrent observations based on a larger sample of targets in future studies. Finally, concerning the variability identified through the multiwavelength polarimetry observations of Mrk 421 and an orphan polarization rotation exhibited by PG1553+113 supports the scenario that the X-ray emission region is separate from that at longer wavelengths.

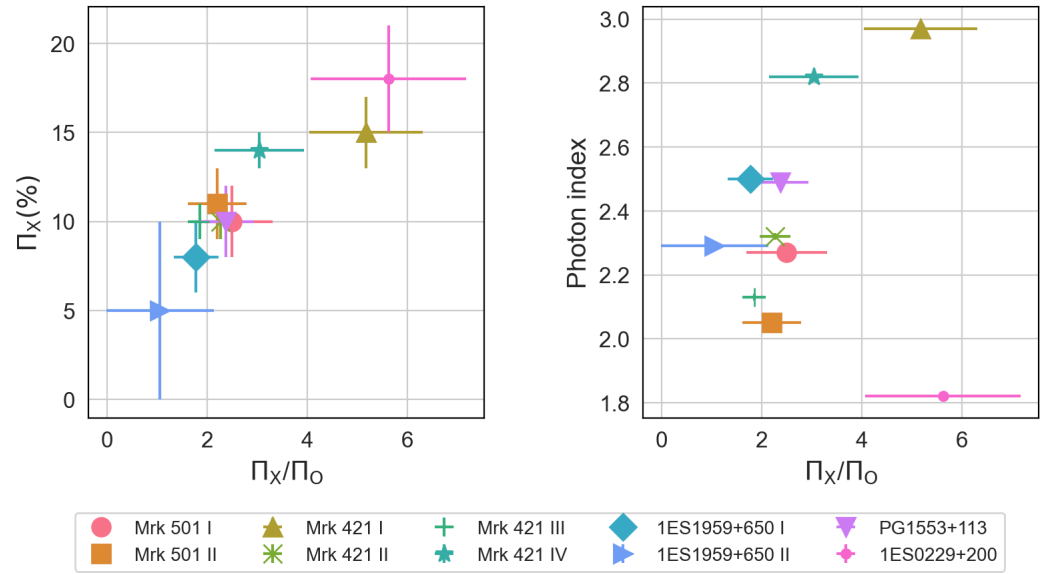


Figure 3. Physical properties of energy-stratified shock emissions from HSP blazars. **(Left)** X-ray polarization vs. the Π_X/Π_O ratio; **(Right)** X-ray power law photon index vs. the Π_X/Π_O ratio of HSP blazars observed by IXPE. Each colored point indicates different IXPE observations labeled in the legend.

2.3. IXPE Observations of Intermediate and Low Synchrotron Peak Blazars

In the case of ISP and LSP blazars, IXPE observations have been carried out for BL Lac [67,68], 3C 273, 3C 279, 3C 454.3, and S5 0716+714 [69]. BL Lac is typically classified as an LSP or ISP, where the Compton hump dominates the soft X-ray band. The X-ray flux and photon index of this target are typically $< 2 \times 10^{-11} \text{ erg s}^{-1}$ and < 2 , respectively. BL Lac has been observed by the IXPE three times: during an average flux state (BL Lac I and II; [62]) and during an outburst (BL Lac III; [67]). From BL Lac I and II, the upper limits of $\Pi_X \leq 14.2\%$ and $\Pi_X \leq 12.6\%$ were estimated, respectively, and the median optical polarization values corresponding to $\Pi_O = 6.8\%$, $\psi_O = 107^\circ$ (during BL Lac I), and $\Pi_O = 14.2\%$ and $\psi_O = 42^\circ$ (during BL Lac II) were measured from contemporaneous multiwavelength polarimetry observations. These results were interpreted as follows: (1) In the leptonic scenario, considering that emission originating from SSC dominates over EC emission in the IXPE energy band according to SED modeling, approximately $\sim 3\%$ of Π_X is predicted from given polarization in radio band, Π_R (BL Lac I $\sim 4\%$ and BL Lac II $\sim 6\%$) [56]. Therefore, the measured X-ray upper limit is consistent with the leptonic scenario. (2) In the hadronic scenario, Π_X similar to or higher than Π_O is predicted, but Π_O was observed to be high. Therefore, the hadronic scenario is disfavored. In conclusion, this disfavors a significant contribution of proton synchrotron radiation to the X-ray emission at these epochs. Instead, it supports a leptonic origin for the X-ray emission in BL Lac.

Furthermore, in the case of BL Lac III, a distinct synchrotron contribution was observed alongside the outburst, with $F_{2-8\text{keV}} = 2.77 \pm 0.21 \times 10^{-11} \text{ erg s}^{-1}$ and a photon index of 2.10 ± 0.09 . Subsequently, Ref. [67] investigated the flux and polarization contributions of the synchrotron emissions across both the soft-energy range (2–4 keV) and the entire IXPE band (2–8 keV) using two power law components. Through time-resolved polarization analysis, dividing the total observation period into three equal sub-periods, a significant X-ray polarization, exceeding 99% significance, with $\Pi_X = 21.7^{+5.6}_{-7.9}$ and $\psi_X = -28.7 \pm 8.7$, was detected only in the first sub-period (upper limits were observed for the remaining sub-periods). This was accompanied by a decrease in the flux contribution of the synchrotron emission component. Moreover, the Π_X value was higher than the concurrently measured $\Pi_O = 13.1 \pm 2.4\%$. These results were explained by the influence of turbulence in the magnetic field, closer to the particle acceleration site in a smaller volume with well-ordered magnetic fields, akin to the characteristics of synchrotron emission observed in HSPs,

leading to the higher Π_X observed in the high-energy regime. Consequently, BL Lac III was concluded to probe the high-frequency end of the synchrotron component, which diminished during the observation.

For the remaining LSP and ISP sources (3C 273, 3C 279, 3C 454.3, and S5 0716+714), only upper limits could be estimated from *IXPE* observations in the 2–8 keV band (3C 273: $\Pi_X < 9.0\%$, 3C 279: $\Pi_X < 12.7\%$, 3C 454.3: $\Pi_X < 28.0\%$, and S5 0716+714: $\Pi_X < 26.0\%$). These observational results, when compared with polarization in the optical and radio domains, suggest that $\Pi_X < \sim 10\%$ and is likely to be less than or comparable to contemporaneous Π_O . Therefore, although hadronic models are not completely eliminated, these X-ray polarization measurements seem to favor the leptonic process, wherein photons are upscattered by relativistic electrons in the jets of blazars. Lastly, Ref. [69] emphasizes that further *IXPE* observations can provide additional insights into the X-ray emission mechanism in LSP and ISP blazars.

3. X-ray Polarization from Hot Coronae

3.1. Theoretical Expectations

The geometry and size of the X-ray corona serve as indicators for exploring its physical origin. The corona could manifest as a slab-like or wedge-like structure originating from the accretion disk, e.g., [30,70], and it could assume a conical shape if it forms the base of a jet, e.g., [29,71,72], or a failed jet, e.g., [28]. Often, it has been assumed for simplicity as a point- or sphere-like configuration located above and below the black hole rotation axis, called lamppost geometry, e.g., [73–75].

The X-ray polarization from the corona is expected to depend on its size, geometry, and position in the system. Recent simulation results using the Monte Carlo Comptonization code (MONK) [76,77] yield the following polarizations for different corona geometries: (1) the slab geometry is predicted to exhibit a maximum polarization, Π_X up to 12%, with ψ_X oriented parallel to the disk axis, i.e., parallel to the direction of the jet; (2) conical geometry is expected to result in ψ_X parallel to the major axis of the projection of the disk on the sky with Π_X up to 7%; (3) in the case of spherical lamppost geometry, Π_X of 1–3% and the same ψ_X as conical geometry are predicted (see Figure 4).

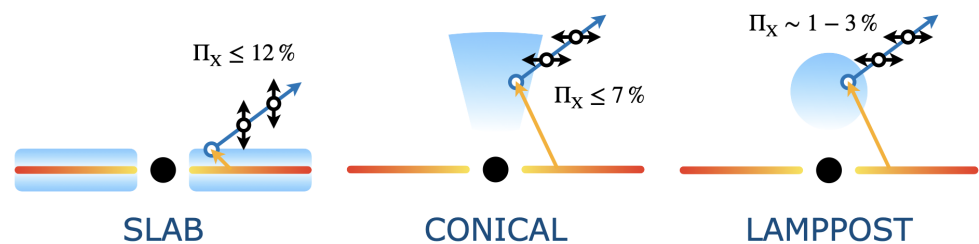


Figure 4. Schematic view of different X-ray corona geometries: slab, conical, and lamppost. The bluish and reddish areas represent the corona and disk emission regions, respectively. Blue and orange arrows indicate upscattered X-ray and UV/optical disk photons, respectively. The black arrow represents the predicted polarization properties (degree in number and angle in direction of the arrow), estimated from [77].

3.2. *IXPE* Observations of Unobscured Radio-Quiet AGN

Since the beginning of *IXPE* operation, three unobscured radio-quiet Seyfert 1 galaxies have been observed (NGC 4151: [78], IC 4329A: [79], and MCG-05-23-16: [80,81]). The X-ray polarization analysis for RQAGN was conducted using both model-independent and spectropolarimetric analysis methods. These methods were employed to examine the time-averaged polarization and the variability in polarization over time and energy. In particular, the relatively more complex spectral features of RQAGN were examined based on simultaneous observations from XMM-Newton and NuSTAR, which cover a wider

energy range with higher spectral resolutions. This allows for a more detailed spectropolarimetric analysis, resulting in the measurement of X-ray polarization characteristics for each emission component. Finally, the polarization properties measured by the IXPE were used to constrain the geometric characteristics of the corona by comparing the expected X-ray polarization results predicted under the different geometrical conditions of the corona with the MONK simulation results.

First, NGC 4151 exhibited X-ray polarization in the 2–8 keV energy range, with $\Pi_X = 4.9 \pm 1.1\%$ and $\psi_X = 86 \pm 7^\circ$ (as shown in the left panel of Figure 5), corresponding to $\sim 4.4\sigma$ significance, as determined by a model-independent polarization analysis. Moreover, NGC 4151 revealed statistically significant variations in the energy-resolved polarization analysis; i.e., we found $\Pi_X = 4.3 \pm 1.6\%$ and $\psi_X = 42 \pm 11^\circ$ in the soft-energy range of 2–3.5 keV, deviating from the measurements in other energy ranges. Additionally, spectropolarimetric analysis (middle panel in Figure 5) takes into account the polarization dilution effect due to the soft-energy regime and sets the polarization angles of the primary emission and reflection emission components perpendicular to each other. As a result, for the primary emission component, $\Pi_X = 7.7 \pm 1.5\%$ and $\psi_X = 87 \pm 6^\circ$ were derived, while, for the reflection component, an upper limit of $\Pi_X < 27\%$ was obtained. Additionally, NGC 4151 exhibits a radio jet feature in VLBI observations [82], and the measured ψ_X shows that it aligns with the direction of the radio jet emission, $\sim 83^\circ$ [83,84]. This indicates that the corona emission originates from the equatorial plane. These polarization results ruled out lamppost and conical geometry scenarios among the proposed coronal geometries. Furthermore, a comparison with the MONK simulations (right panel in Figure 5) confirmed that the IXPE observational results agree well with the predicted polarization results from the slab or wedge geometry. Moreover, the observed ψ_X in the soft-energy band is similar to that of the extended narrow-line region (NLR), with a confirmed orientation by HST [85,86], supported by a Chandra observation [87] value of $45 \pm 5^\circ$, suggesting that a new emission component may influence the X-ray polarization, which is to be confirmed through additional observations.

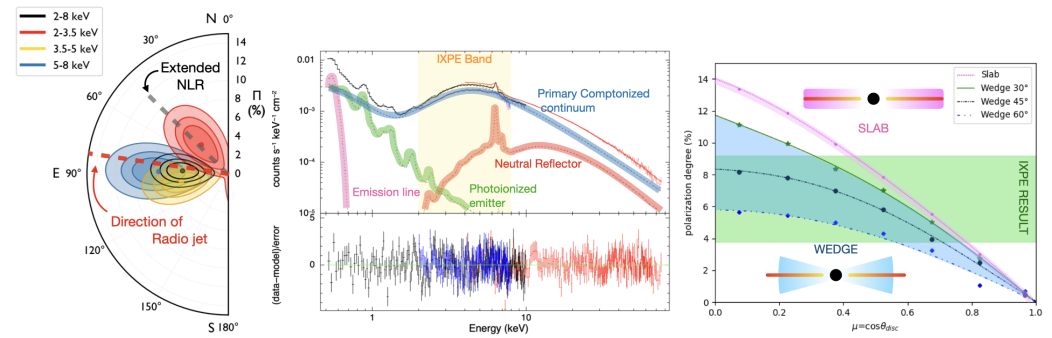


Figure 5. IXPE observation result of NGC 4151. **(Left)** Polarization contours (68%, 90%, and 99% detection significance levels); **(middle)** X-ray spectrum analysis result; **(right)** comparison of IXPE measurements and expected X-ray polarization in slab and wedge geometry coronae calculated from MONK simulations. The figure was reproduced with kind permission from Oxford University Press and the Royal Astronomical Society from [78].

Next, MCG-05-23-16 underwent two observations (MCG-05-23-16 I: May 2022 and MCG-05-23-16 II: November 2022), yielding upper limits of $\Pi_X \leq 4.7\%$ and $\Pi_X \leq 3.3\%$, respectively. The integrated analysis of MCG-05-23-16 I and II resulted in an upper limit of $\Pi_X < 3.2\%$, and Figure 6 illustrates the comparison of the X-ray polarization contour plot with the predicted polarization characteristics from the MONK simulations of the proposed corona geometries. Thus, despite ψ being estimated at a $\sim 1\sigma$ confidence level, considering the direction of the NLR estimated by the HST [O III] emission observations to be $\sim 40^\circ$ [88], and taking into account the perpendicular orientation of the NLR and the accretion disk, the results hint at a coronal geometry in the form of a slab or wedge rather than a

lamppost or conical shape. Additionally, the disk inclination estimated in [89] of $\sim 30\text{--}50^\circ$ supports the results of a coronal structure like a slab or wedge.

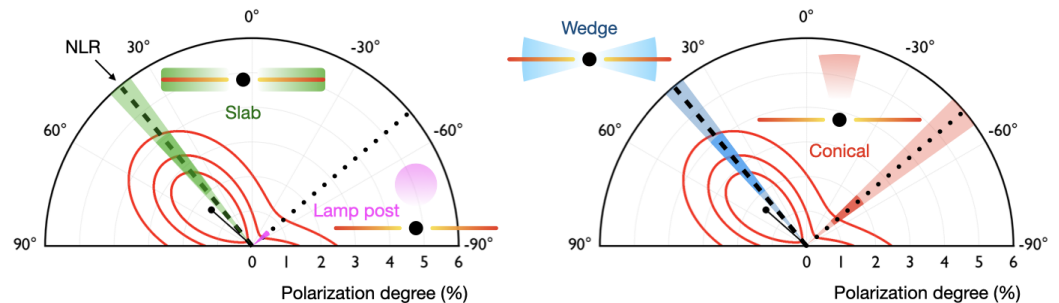


Figure 6. X-ray polarization contours of the integrated analysis of MCG-05-23-16 I and II (red; 68%, 90%, and 99% detection significance levels). The black dashed line indicates the direction of the NLR, while the dotted line denotes the perpendicular direction, implying an angle parallel to the disk. Each colored area represents the expected polarization properties calculated by MONK, with relatively saturated regions indicating the expected degree of polarization for inclinations in the range of approximately $30\text{--}50^\circ$. The figure was reproduced with kind permission from Oxford University Press and the Royal Astronomical Society from Figure 8 in [80].

Finally, IC 4329A has a detected X-ray polarization of the hot corona of $3.3 \pm 1.1\%$ for Π_X and $78 \pm 10^\circ$ for ψ_X in the 2–8 keV band, utilizing simultaneous observational data from IXPE, XMM-Newton, and NuSTAR for the spectropolarimetric analysis. For the spectral model, a Comptonization and a reflection component have been applied. The ψ_X was roughly aligned with the position angle of the extended radio emission at $\sim 90^\circ$, e.g., [90]. This result, consistent with NGC 4151 and MCG-05-23-16, supports the geometric properties of a radially extended corona within the plane of the disk. Additionally, in [79], through a more detailed examination using MONK simulations, a test of the slab and wedge geometry corona system has been conducted. This tentatively suggests, at a 90% confidence level, a lower limit for Π_X , favoring asymmetric configurations possibly characterized by outflowing coronal geometries extended within the disk plane, which would generate highly polarized emissions aligned with the jet.

4. Summary

The IXPE mission has pioneered X-ray polarimetry, achieving the first-ever detections of X-ray polarization from AGN. The diverse physical characteristics of AGN observed in the X-ray range, particularly in the RLAGN population represented by blazars and the RQAGN population represented by unobscured RQAGN, have provided crucial insights into estimating the particle acceleration processes within relativistic jets, the physical and geometrical properties of magnetic fields, and the intrinsic geometry of hot coronae. The IXPE observations of blazars, notably the HSP subclass starting with the first observation of Mrk 501, are consistent with the possibility that the synchrotron emission within the jet originates from energy-stratified shocks. Subsequent observations of Mrk 421 have further supported this scenario and indicated the presence of helical magnetic fields by discovering the smooth rotation of the polarization angle for the first time in the X-ray range. Additionally, other HSP observations, including 1ES1959+650, PG1553+113, and 1ES0229+200, showed values of the Π_X/Π_O ratio around $\sim 2\text{--}6$, supporting the conclusions drawn from Mrk501 and Mrk421. Furthermore, extensive comparisons of all the HSP observations have led to a physical interpretation suggesting that synchrotron jet emission at high frequencies takes place in environments with smaller volumes of well-ordered magnetic fields close to shock fronts. The polarization information at longer wavelengths is diluted by magnetic field turbulence. This interpretation could gain further solidity

through additional IXPE observations focusing on spectral properties and polarization angles. Furthermore, temporal variations in polarization properties have been solidly observed only in Mrk 421 to date. Hence, the characteristic of significant polarization variability observed only in specific targets should be meticulously investigated in future studies, considering additional parameters such as the physical characteristics of the jet and utilizing more extensive observational data. Lastly, the individual variations in polarization observed across multiple wavelengths imply spatial segregation between X-ray emissions and emissions at other wavelengths.

IXPE observations of other subclasses of blazars, including LSPs and ISPs, were carried out to explore the particle acceleration mechanisms of the Inverse Compton emission component situated in the jet's higher-energy band. The observations of BL Lac objects confirmed that the polarization characteristics predicted by the leptonic-based SSC acceleration mechanisms better explain the IXPE observations than hadronic scenarios. However, the relatively low X-ray flux compared to HSPs poses challenges in achieving statistically significant observational results for many targets. Thus, further exploration through observations during higher-source activity states such as future outbursts or longer exposure times should be considered.

The IXPE observations of RQAGN explore the geometry of the X-ray corona centered around the unobscured central engine. Observations of NGC4151, MCG-05-23-16, and IC4329A with IXPE detected polarization within 3–5% from the coronal emission, aligned with the inferred jet direction. These results suggest that the corona, instead of being located on the black hole axis as expected if it is the base or possibly failed jet, is better explained by a slab-like or wedge-like shape, believed to originate from Comptonization around the accretion disk, such as a disk outflow. The IXPE findings were further validated through a comparison with the predicted X-ray polarization characteristics calculated via MONK simulations based on various geometrical structures. Furthermore, observations of NGC 4151 suggested the possibility of other emission components in the soft-energy band influencing the X-ray polarization, a characteristic that will be further explored in depth through future additional IXPE observations. Finally, future IXPE observations aimed at probing the different states of the corona emission process and reflection emission in the accretion disk will provide additional evidence to expand our understanding of the physical emission processes occurring inside AGN.

Author Contributions: Conceptualization, formal analysis, visualization, and writing—original draft preparation, D.E.K.; writing—review and editing, L.D.G., F.M., A.P.M., G.M., P.S., F.T., E.C. and I.D. All authors have read and agreed to the published version of the manuscript.

Funding: The Imaging X-ray Polarimetry Explorer (IXPE) is a joint US and Italian mission. The US contribution is supported by the National Aeronautics and Space Administration (NASA) and led and managed by its Marshall Space Flight Center (MSFC), with industry partner Ball Aerospace (contract NNM15AA18C). The Italian contribution is supported by the Italian Space Agency (Agenzia Spaziale Italiana, ASI) through contract ASI-OHBI-2017-12-I.0, agreements ASI-INAF-2017-12-H0 and ASI-INFN-2017.13-H0, and its Space Science Data Center (SSDC), and by the Istituto Nazionale di Astrofisica (INAF) and the Istituto Nazionale di Fisica Nucleare (INFN) in Italy. This research used data products provided by the IXPE Team (MSFC, SSDC, INAF, and INFN) and distributed with additional software tools by the High-Energy Astrophysics Science Archive Research Center (HEASARC) at NASA Goddard Space Flight Center (GSFC). The research of APM was partially supported by National Science Foundation grant AST-2108622, NASA Swift grant 80NSSC23K1145, and NASA NuSTAR grant 80NSSC22K0537.

Data Availability Statement: IXPE data are publicly available at <https://heasarc.gsfc.nasa.gov/docs/heasarc/missions/ixpe.html> (accessed on 17 March 2024).

Conflicts of Interest: The authors declare no conflict of interest.

References

1. Woo, J.H.; Urry, C.M. Active Galactic Nucleus Black Hole Masses and Bolometric Luminosities. *Astrophys. J.* **2002**, *579*, 530–544. <https://doi.org/10.1086/342878>.
2. Perna, M.; Lanzuisi, G.; Brusa, M.; Mignoli, M.; Cresci, G. An X-ray/SDSS sample. I. Multi-phase outflow incidence and dependence on AGN luminosity. *Astron. Astrophys.* **2017**, *603*, A99. <https://doi.org/10.1051/0004-6361/201630369>.
3. Bambi, C.; Sanganelo, A. *Handbook of X-ray and GAMMA-ray Astrophysics*; Springer: Singapore, 2022.
4. Rybicki, G.B.; Lightman, A.P. *Radiative Processes in Astrophysics*; John Wiley & Sons: Hoboken, NJ, USA, 1979.
5. Weisskopf, M.C.; Soffitta, P.; Baldini, L.; Ramsey, B.D.; O'Dell, S.L.; Romani, R.W.; Matt, G.; Deinger, W.D.; Baumgartner, W.H.; Bellazzini, R.; et al. The Imaging X-ray Polarimetry Explorer (IXPE): Pre-Launch. *J. Astron. Telesc. Instrum. Syst.* **2022**, *8*, 026002. <https://doi.org/10.1117/1.JATIS.8.2.026002>.
6. Costa, E.; Soffitta, P.; Bellazzini, R.; Brez, A.; Lumb, N.; Spandre, G. An efficient photoelectric X-ray polarimeter for the study of black holes and neutron stars. *Nature* **2001**, *411*, 662–665. <https://doi.org/10.1038/35079508>.
7. Urry, C.M.; Padovani, P. Unified Schemes for Radio-Loud Active Galactic Nuclei. *Publ. Astron. Soc. Pac.* **1995**, *107*, 803. <https://doi.org/10.1086/133630>.
8. Padovani, P.; Alexander, D.M.; Assef, R.J.; De Marco, B.; Giommi, P.; Hickox, R.C.; Richards, G.T.; Smolčić, V.; Hatziminaoglou, E.; Mainieri, V.; et al. Active galactic nuclei: what's in a name? *Astron. Astrophys. Rev.* **2017**, *25*, 2. <https://doi.org/10.1007/s00159-017-0102-9>.
9. Padovani, P. On the two main classes of active galactic nuclei. *Nat. Astron.* **2017**, *1*, 0194. <https://doi.org/10.1038/s41550-017-0194>.
10. Hovatta, T.; Lindfors, E.; Blinov, D.; Pavlidou, V.; Nilsson, K.; Kiehlmann, S.; Angelakis, E.; Fallah Ramazani, V.; Lioudakis, I.; Myserlis, I.; et al. Optical polarization of high-energy BL Lacertae objects. *Astron. Astrophys.* **2016**, *596*, A78. <https://doi.org/10.1051/0004-6361/201628974>.
11. Jones, T.W.; O'Dell, S.L.; Stein, W.A. Physics of Compact Nonthermal Sources. I. Theory of Radiation Processes. *Astrophys. J.* **1974**, *188*, 353–368. <https://doi.org/10.1086/152724>.
12. Maraschi, L.; Ghisellini, G.; Celotti, A. A Jet Model for the Gamma-Ray-emitting Blazar 3C 279. *Astrophys. J. Lett.* **1992**, *397*, L5. <https://doi.org/10.1086/186531>.
13. Dermer, C.D.; Schlickeiser, R. Model for the High-Energy Emission from Blazars. *Astrophys. J.* **1993**, *416*, 458. <https://doi.org/10.1086/173251>.
14. Sikora, M.; Begelman, M.C.; Rees, M.J. Comptonization of Diffuse Ambient Radiation by a Relativistic Jet: The Source of Gamma Rays from Blazars? *Astrophys. J.* **1994**, *421*, 153. <https://doi.org/10.1086/173633>.
15. Begelman, M.C.; Sikora, M. Inverse Compton Scattering of Ambient Radiation by a Cold Relativistic Jet: A Source of Beamed, Polarized X-ray and Optical Observations of X-ray-selected BL Lacertae Objects. *Astrophys. J.* **1987**, *322*, 650. <https://doi.org/10.1086/165760>.
16. Mannheim, K. The proton blazar. *Astron. Astrophys.* **1993**, *269*, 67–76. <https://doi.org/10.48550/arXiv.astro-ph/9302006>.
17. Aharonian, F.A. TeV gamma rays from BL Lac objects due to synchrotron radiation of extremely high energy protons. *New Astron.* **2000**, *5*, 377–395. [https://doi.org/10.1016/S1384-1076\(00\)00039-7](https://doi.org/10.1016/S1384-1076(00)00039-7).
18. Böttcher, M.; Reimer, A.; Sweeney, K.; Prakash, A. Leptonic and Hadronic Modeling of Fermi-detected Blazars. *Astrophys. J.* **2013**, *768*, 54. <https://doi.org/10.1088/0004-637X/768/1/54>.
19. Blandford, R.; Meier, D.; Readhead, A. Relativistic Jets from Active Galactic Nuclei. *Annu. Rev. Astron. Astrophys.* **2019**, *57*, 467–509. <https://doi.org/10.1146/annurev-astro-081817-051948>.
20. Abdo, A.A.; Ackermann, M.; Agudo, I.; Ajello, M.; Aller, H.D.; Aller, M.F.; Angelakis, E.; Arkharov, A.A.; Axelsson, M.; Bach, U.; et al. The Spectral Energy Distribution of Fermi Bright Blazars. *Astrophys. J.* **2010**, *716*, 30–70. <https://doi.org/10.1088/0004-637X/716/1/30>.
21. Haardt, F.; Maraschi, L. A Two-Phase Model for the X-ray Emission from Seyfert Galaxies. *Astrophys. J. Lett.* **1991**, *380*, L51. <https://doi.org/10.1086/186171>.
22. Marin, F.; Dovčiak, M.; Kammoun, E.S. Contribution of parsec-scale material on to the polarized X-ray spectrum of type 1 Seyfert galaxies. *Mon. Not. R. Astron. Soc.* **2018**, *478*, 950–960. <https://doi.org/10.1093/mnras/sty1062>.
23. Antonucci, R. Unified models for active galactic nuclei and quasars. *Annu. Rev. Astron. Astrophys.* **1993**, *31*, 473–521. <https://doi.org/10.1146/annurev.aa.31.090193.002353>.
24. Wu, X.B.; Han, J.L. Inclinations and Black Hole Masses of Seyfert 1 Galaxies. *Astrophys. J. Lett.* **2001**, *561*, L59–L62. <https://doi.org/10.1086/324408>.
25. Singha, M.; Husemann, B.; Urrutia, T.; O'Dea, C.P.; Scharwächter, J.; Gaspari, M.; Combes, F.; Nevin, R.; Terrazas, B.A.; Pérez-Torres, M.; et al. The Close AGN Reference Survey (CARS). Locating the [O III] wing component in luminous local Type 1 AGN. *Astron. Astrophys.* **2022**, *659*, A123. <https://doi.org/10.1051/0004-6361/202040122>.
26. Sunyaev, R.A.; Titarchuk, L.G. Comptonization of X-rays in Plasma Clouds - Typical Radiation Spectra. *Astron. Astrophys.* **1980**, *86*, 121.
27. Di Matteo, T. Magnetic reconnection: flares and coronal heating in active galactic nuclei. *Mon. Not. R. Astron. Soc.* **1998**, *299*, L15–L20. <https://doi.org/10.1046/j.1365-8711.1998.01950.x>.

28. Ghisellini, G.; Haardt, F.; Matt, G. Aborted jets and the X-ray emission of radio-quiet AGNs. *Astron. Astrophys.* **2004**, *413*, 535–545. <https://doi.org/10.1051/0004-6361:20031562>.
29. Markoff, S.; Nowak, M.A.; Wilms, J. Going with the Flow: Can the Base of Jets Subsume the Role of Compact Accretion Disk Coronae? *Astrophys. J.* **2005**, *635*, 1203–1216. <https://doi.org/10.1086/497628>.
30. Haardt, F.; Matt, G. X-ray polarization in the two-phase model for AGN and X-ray binaries. *Mon. Not. R. Astron. Soc.* **1993**, *261*, 346–352. <https://doi.org/10.1093/mnras/261.2.346>.
31. Matt, G.; Perola, G.C.; Costa, E.; Piro, L. X-ray polarization of the reprocessed emission from accretion disk in Seyfert galaxies. In *Two Topics in X-ray Astronomy, Volume 1: X Ray Binaries. Volume 2: AGN and the X Ray Background*; Hunt, J., Battrick, B., Eds.; ESA Special Publication: 1989, Volume 296, pp. 991–993.
32. Matt, G.; Fabian, A.C.; Ross, R.R. X-ray photoionized accretion discs: UV and X-ray continuum spectra and polarization. *Mon. Not. R. Astron. Soc.* **1993**, *264*, 839–852. <https://doi.org/10.1093/mnras/264.4.839>.
33. Jorstad, S.G.; Marscher, A.P.; Lister, M.L.; Stirling, A.M.; Cawthorne, T.V.; Gear, W.K.; Gómez, J.L.; Stevens, J.A.; Smith, P.S.; Forster, J.R.; et al. Polarimetric Observations of 15 Active Galactic Nuclei at High Frequencies: Jet Kinematics from Bimonthly Monitoring with the Very Long Baseline Array. *Astron. J.* **2005**, *130*, 1418–1465. <https://doi.org/10.1086/444593>.
34. Kiehlmann, S.; Blinov, D.; Pearson, T.J.; Lioudakis, I. Optical EVPA rotations in blazars: testing a stochastic variability model with RoboPol data. *Mon. Not. R. Astron. Soc.* **2017**, *472*, 3589–3604. <https://doi.org/10.1093/mnras/stx2167>.
35. Blinov, D.; Pavlidou, V.; Papadakis, I.; Kiehlmann, S.; Lioudakis, I.; Panopoulou, G.V.; Angelakis, E.; Baloković, M.; Hovatta, T.; King, O.G.; et al. RoboPol: connection between optical polarization plane rotations and gamma-ray flares in blazars. *Mon. Not. R. Astron. Soc.* **2018**, *474*, 1296–1306. <https://doi.org/10.1093/mnras/stx2786>.
36. Larionov, V.M.; Jorstad, S.G.; Marscher, A.P.; Morozova, D.A.; Blinov, D.A.; Hagen-Thorn, V.A.; Konstantinova, T.S.; Kopatskaya, E.N.; Larionova, L.V.; Larionova, E.G.; et al. The Outburst of the Blazar S5 0716+71 in 2011 October: Shock in a Helical Jet. *Astrophys. J.* **2013**, *768*, 40. <https://doi.org/10.1088/0004-637X/768/1/40>.
37. Marscher, A.P.; Jorstad, S.G.; D’Arcangelo, F.D.; Smith, P.S.; Williams, G.G.; Larionov, V.M.; Oh, H.; Olmstead, A.R.; Aller, M.F.; Aller, H.D.; et al. The inner jet of an active galactic nucleus as revealed by a radio-to- γ -ray outburst. *Nature* **2008**, *452*, 966–969. <https://doi.org/10.1038/nature06895>.
38. Lyutikov, M.; Kravchenko, E.V. Polarization swings in blazars. *Mon. Not. R. Astron. Soc.* **2017**, *467*, 3876–3886. <https://doi.org/10.1093/mnras/stx359>.
39. Marscher, A.P. Turbulent, Extreme Multi-zone Model for Simulating Flux and Polarization Variability in Blazars. *Astrophys. J.* **2014**, *780*, 87. <https://doi.org/10.1088/0004-637X/780/1/87>.
40. Marscher, A.P.; Jorstad, S.G.; Williamson, K.E. Modeling the Time-Dependent Polarization of Blazars. *Galaxies* **2017**, *5*, 63. <https://doi.org/10.3390/galaxies5040063>.
41. Marscher, A.P.; Jorstad, S.G. Frequency and Time Dependence of Linear Polarization in Turbulent Jets of Blazars. *Galaxies* **2021**, *9*, 27. <https://doi.org/10.3390/galaxies9020027>.
42. Achterberg, A.; Gallant, Y.A.; Kirk, J.G.; Guthmann, A.W. Particle acceleration by ultrarelativistic shocks: theory and simulations. *Mon. Not. R. Astron. Soc.* **2001**, *328*, 393–408. <https://doi.org/10.1046/j.1365-8711.2001.04851.x>.
43. Spitkovsky, A. Particle Acceleration in Relativistic Collisionless Shocks: Fermi Process at Last? *Astrophys. J.* **2008**, *682*, L5. <https://doi.org/10.1086/590248>.
44. Mizuno, Y.; Lyubarsky, Y.; Nishikawa, K.I.; Hardee, P.E. Three-Dimensional Relativistic Magnetohydrodynamic Simulations of Current-Driven Instability. I. Instability of a Static Column. *Astrophys. J.* **2009**, *700*, 684–693. <https://doi.org/10.1088/0004-637X/700/1/684>.
45. Alves, E.P.; Zrake, J.; Fiuza, F. Efficient Nonthermal Particle Acceleration by the Kink Instability in Relativistic Jets. *Phys. Rev. Lett.* **2018**, *121*, 245101. <https://doi.org/10.1103/PhysRevLett.121.245101>.
46. Sironi, L.; Spitkovsky, A. Relativistic Reconnection: An Efficient Source of Non-thermal Particles. *Astrophys. J. Lett.* **2014**, *783*, L21. <https://doi.org/10.1088/2041-8205/783/1/L21>.
47. Guo, F.; Li, H.; Daughton, W.; Liu, Y.H. Formation of Hard Power Laws in the Energetic Particle Spectra Resulting from Relativistic Magnetic Reconnection. *Phys. Rev. Lett.* **2014**, *113*, 155005. <https://doi.org/10.1103/PhysRevLett.113.155005>.
48. Zhang, H.; Li, X.; Guo, F.; Giannios, D. Large-amplitude Blazar Polarization Angle Swing as a Signature of Magnetic Reconnection. *Astrophys. J. Lett.* **2018**, *862*, L25. <https://doi.org/10.3847/2041-8213/aad54f>.
49. Zhang, H.; Li, X.; Giannios, D.; Guo, F.; Thiersen, H.; Böttcher, M.; Lewis, T.; Venters, T. Radiation and Polarization Signatures from Magnetic Reconnection in Relativistic Jets. II. Connection with γ -Rays. *Astrophys. J.* **2022**, *924*, 90. <https://doi.org/10.3847/1538-4357/ac3669>.
50. Tavecchio, F. Probing Magnetic Fields and Acceleration Mechanisms in Blazar Jets with X-ray Polarimetry. *Galaxies* **2021**, *9*, 37. <https://doi.org/10.3390/galaxies9020037>.
51. Di Gesu, L.; Tavecchio, F.; Donnarumma, I.; Marscher, A.; Pesce-Rollins, M.; Landoni, M. Testing particle acceleration models for BL Lac jets with the Imaging X-ray Polarimetry Explorer. *Astron. Astrophys.* **2022**, *662*, A83. <https://doi.org/10.1051/0004-6361/202243168>.
52. Tavecchio, F.; Landoni, M.; Sironi, L.; Coppi, P. Probing shock acceleration in BL Lac jets through X-ray polarimetry: the time-dependent view. *Mon. Not. R. Astron. Soc.* **2020**, *498*, 599–608. <https://doi.org/10.1093/mnras/staa2457>.

53. Tavecchio, F.; Landoni, M.; Sironi, L.; Coppi, P. Probing dissipation mechanisms in BL Lac jets through X-ray polarimetry. *Mon. Not. R. Astron. Soc.* **2018**, *480*, 2872–2880. <https://doi.org/10.1093/mnras/sty1491>.
54. Guo, F.; Liu, Y.H.; Daughton, W.; Li, H. Particle Acceleration and Plasma Dynamics during Magnetic Reconnection in the Magnetically Dominated Regime. *Astrophys. J.* **2015**, *806*, 167. <https://doi.org/10.1088/0004-637X/806/2/167>.
55. Zhang, H.; Böttcher, M. X-ray and Gamma-Ray Polarization in Leptonic and Hadronic Jet Models of Blazars. *Astrophys. J.* **2013**, *774*, 18. <https://doi.org/10.1088/0004-637X/774/1/18>.
56. Peirson, A.L.; Romani, R.W. The Polarization Behavior of Relativistic Synchrotron Self-Compton Jets. *Astrophys. J.* **2019**, *885*, 76. <https://doi.org/10.3847/1538-4357/ab46b1>.
57. Liodakis, I.; Marscher, A.P.; Agudo, I.; Berdyugin, A.V.; Bernardos, M.I.; Bonnoli, G.; Borman, G.A.; Casadio, C.; Casanova, V.; Cavazzuti, E.; et al. Polarized blazar X-rays imply particle acceleration in shocks. *Nature* **2022**, *611*, 677–681. <https://doi.org/10.1038/s41586-022-05338-0>.
58. Di Gesu, L.; Donnarumma, I.; Tavecchio, F.; Agudo, I.; Barnounin, T.; Cibrario, N.; Di Lalla, N.; Di Marco, A.; Escudero, J.; Errando, M.; et al. The X-ray Polarization View of Mrk 421 in an Average Flux State as Observed by the Imaging X-ray Polarimetry Explorer. *Astrophys. J. Lett.* **2022**, *938*, L7. <https://doi.org/10.3847/2041-8213/ac913a>.
59. Di Gesu, L.; Marshall, H.L.; Ehlert, S.R.; Kim, D.E.; Donnarumma, I.; Tavecchio, F.; Liodakis, I.; Kiehlmann, S.; Agudo, I.; Jorstad, S.G.; et al. Discovery of X-ray polarization angle rotation in the jet from blazar Mrk 421. *Nat. Astron.* **2023**, *7*, 1245–1258. <https://doi.org/10.1038/s41550-023-02032-7>.
60. Kim, D.E.; Di Gesu, L.; Liodakis, I.; Marscher, A.P.; Jorstad, S.G.; Middei, R.; Marshall, H.L.; Pacciani, L.; Agudo, I.; Tavecchio, F.; et al. Magnetic field properties inside the jet of Mrk 421. Multiwavelength polarimetry, including the Imaging X-ray Polarimetry Explorer. *Astron. Astrophys.* **2024**, *681*, A12. <https://doi.org/10.1051/0004-6361/202347408>.
61. Errando, M.; Liodakis, I.; Marscher, A.P.; Marshall, H.L.; Middei, R.; Negro, M.; Peirson, A.L.; Perri, M.; Puccetti, S.; Rabinowitz, P.L.; et al. Detection of X-ray Polarization from the Blazar 1ES 1959+650 with the Imaging X-ray Polarimetry Explorer. *arXiv* **2024**, arXiv:2401.04420. <https://doi.org/10.48550/arXiv.2401.04420>.
62. Middei, R.; Perri, M.; Puccetti, S.; Liodakis, I.; Di Gesu, L.; Marscher, A.P.; Rodriguez Caverio, N.; Tavecchio, F.; Donnarumma, I.; Laurenti, M.; et al. IXPE and Multiwavelength Observations of Blazar PG 1553+113 Reveal an Orphan Optical Polarization Swing. *Astrophys. J. Lett.* **2023**, *953*, L28. <https://doi.org/10.3847/2041-8213/acec3e>.
63. Ehlert, S.R.; Liodakis, I.; Middei, R.; Marscher, A.P.; Tavecchio, F.; Agudo, I.; Kouch, P.M.; Lindfors, E.; Nilsson, K.; Myserlis, I.; et al. X-ray Polarization of the BL Lacertae Type Blazar 1ES 0229+200. *Astrophys. J.* **2023**, *959*, 61. <https://doi.org/10.3847/1538-4357/ad05c4>.
64. Kislat, F.; Clark, B.; Beilicke, M.; Krawczynski, H. Analyzing the data from X-ray polarimeters with Stokes parameters. *Astroparticle Physics* **2015**, *68*, 45–51. [arXiv:astro-ph.IM/1409.6214]. <https://doi.org/10.1016/j.astropartphys.2015.02.007>.
65. Strohmayer, T.E. X-ray Spectro-polarimetry with Photoelectric Polarimeters. *Astrophys. J.* **2017**, *838*, 72. <https://doi.org/10.3847/1538-4357/aa643d>.
66. Massaro, E.; Perri, M.; Giommi, P.; Nesci, R. Log-parabolic spectra and particle acceleration in the BL Lac object Mkn 421: Spectral analysis of the complete BeppoSAX wide band X-ray data set. *Astron. Astrophys.* **2004**, *413*, 489–503. <https://doi.org/10.1051/0004-6361:20031558>.
67. Peirson, A.L.; Negro, M.; Liodakis, I.; Middei, R.; Kim, D.E.; Marscher, A.P.; Marshall, H.L.; Pacciani, L.; Romani, R.W.; Wu, K.; et al. X-ray Polarization of BL Lacertae in Outburst. *Astrophys. J. Lett.* **2023**, *948*, L25. <https://doi.org/10.3847/2041-8213/acd242>.
68. Middei, R.; Liodakis, I.; Perri, M.; Puccetti, S.; Cavazzuti, E.; Di Gesu, L.; Ehlert, S.R.; Madejski, G.; Marscher, A.P.; Marshall, H.L.; et al. X-ray Polarization Observations of BL Lacertae. *Astrophys. J. Lett.* **2023**, *942*, L10. <https://doi.org/10.3847/2041-8213/aca281>.
69. Marshall, H.L.; Liodakis, I.; Marscher, A.P.; Di Lalla, N.; Jorstad, S.G.; Kim, D.E.; Middei, R.; Negro, M.; Omodei, N.; Peirson, A.L.; et al. Observations of Low and Intermediate Spectral Peak Blazars with the Imaging X-ray Polarimetry Explorer. *arXiv* **2023**, arXiv:2310.11510. <https://doi.org/10.48550/arXiv.2310.11510>.
70. Poutanen, J.; Veledina, A.; Beloborodov, A.M. Polarized X-rays from Windy Accretion in Cygnus X-1. *Astrophys. J. Lett.* **2023**, *949*, L10. <https://doi.org/10.3847/2041-8213/acd33e>.
71. Henri, G.; Pelletier, G. Relativistic Electron-Positron Beam Formation in the Framework of the Two-Flow Model for Active Galactic Nuclei. *Astrophys. J. Lett.* **1991**, *383*, L7. <https://doi.org/10.1086/186228>.
72. Henri, G.; Petrucci, P.O. Anisotropic illumination of AGN's accretion disk by a non thermal source. I. General theory and application to the Newtonian geometry. *Astron. Astrophys.* **1997**, *326*, 87–98. <https://doi.org/10.48550/arXiv.astro-ph/9705233>.
73. Martocchia, A.; Matt, G. Iron K α line intensity from accretion discs around rotating black holes. *Mon. Not. R. Astron. Soc.* **1996**, *282*, L53–L57. <https://doi.org/10.1093/mnras/282.4.L53>.
74. Miniutti, G.; Fabian, A.C. A light bending model for the X-ray temporal and spectral properties of accreting black holes. *Mon. Not. R. Astron. Soc.* **2004**, *349*, 1435–1448. <https://doi.org/10.1111/j.1365-2966.2004.07611.x>.
75. Wilkins, D.R.; Fabian, A.C. Understanding X-ray reflection emissivity profiles in AGN: locating the X-ray source. *Mon. Not. R. Astron. Soc.* **2012**, *424*, 1284–1296. <https://doi.org/10.1111/j.1365-2966.2012.21308.x>.
76. Zhang, W.; Dovčiak, M.; Bursa, M. Constraining the Size of the Corona with Fully Relativistic Calculations of Spectra of Extended Coronae. I. The Monte Carlo Radiative Transfer Code. *Astrophys. J.* **2019**, *875*, 148. <https://doi.org/10.3847/1538-4357/ab1261>.

77. Ursini, F.; Matt, G.; Bianchi, S.; Marinucci, A.; Dovčiak, M.; Zhang, W. Prospects for differentiating extended coronal geometries in AGNs with the IXPE mission. *Mon. Not. R. Astron. Soc.* **2022**, *510*, 3674–3687. <https://doi.org/10.1093/mnras/stab3745>.
78. Gianolli, V.E.; Kim, D.E.; Bianchi, S.; Agis-González, B.; Madejski, G.; Marin, F.; Marinucci, A.; Matt, G.; Middei, R.; Petrucci, P.O.; et al. Uncovering the geometry of the hot X-ray corona in the Seyfert galaxy NGC 4151 with IXPE. *Mon. Not. R. Astron. Soc.* **2023**, *523*, 4468–4476. <https://doi.org/10.1093/mnras/stad1697>.
79. Ingram, A.; Ewing, M.; Marinucci, A.; Tagliacozzo, D.; Rosario, D.J.; Veledina, A.; Kim, D.E.; Marin, F.; Bianchi, S.; Poutanen, J.; et al. The X-ray polarization of the Seyfert 1 galaxy IC 4329A. *Mon. Not. R. Astron. Soc.* **2023**, *525*, 5437–5449. <https://doi.org/10.1093/mnras/stad2625>.
80. Tagliacozzo, D.; Marinucci, A.; Ursini, F.; Matt, G.; Bianchi, S.; Baldini, L.; Barnouin, T.; Cavero Rodriguez, N.; De Rosa, A.; Di Gesu, L.; et al. The geometry of the hot corona in MCG-05-23-16 constrained by X-ray polarimetry. *Mon. Not. R. Astron. Soc.* **2023**, *525*, 4735–4743. <https://doi.org/10.1093/mnras/stad2627>.
81. Marinucci, A.; Muleri, F.; Dovciak, M.; Bianchi, S.; Marin, F.; Matt, G.; Ursini, F.; Middei, R.; Marshall, H.L.; Baldini, L.; et al. Polarization constraints on the X-ray corona in Seyfert Galaxies: MCG-05-23-16. *Mon. Not. R. Astron. Soc.* **2022**, *516*, 5907–5913. <https://doi.org/10.1093/mnras/stac2634>.
82. Williams, D.R.A.; McHardy, I.M.; Baldi, R.D.; Beswick, R.J.; Argo, M.K.; Dullo, B.T.; Knapen, J.H.; Brinks, E.; Fenech, D.M.; Mundell, C.G.; et al. Radio jets in NGC 4151: where eMERLIN meets HST. *Mon. Not. R. Astron. Soc.* **2017**, *472*, 3842–3853. <https://doi.org/10.1093/mnras/stx2205>.
83. Harrison, B.; Pedlar, A.; Unger, S.W.; Burgess, P.; Graham, D.A.; Preuss, E. The parsec-scale structure of the radio nucleus of NGC 4151. *Mon. Not. R. Astron. Soc.* **1986**, *218*, 775–784. <https://doi.org/10.1093/mnras/218.4.775>.
84. Ulvestad, J.S.; Roy, A.L.; Colbert, E.J.M.; Wilson, A.S. A Subparsec Radio Jet or Disk in NGC 4151. *Astrophys. J.* **1998**, *496*, 196–202. <https://doi.org/10.1086/305382>.
85. Evans, I.N.; Tsvetanov, Z.; Kriss, G.A.; Ford, H.C.; Caganoff, S.; Koratkar, A.P. Hubble Space Telescope Imaging of the Narrow-Line Region of NGC 4151. *Astrophys. J.* **1993**, *417*, 82. <https://doi.org/10.1086/173292>.
86. Das, V.; Crenshaw, D.M. Mapping the Kinematics of the Narrow-Line Regions in NGC 4151 and NGC 1068. In *American Astronomical Society Meeting Abstracts*; 2003; Volume 203, p. 56.01.
87. Wang, J.; Fabbiano, G.; Elvis, M.; Risaliti, G.; Karovska, M.; Zezas, A.; Mundell, C.G.; Dumas, G.; Schinnerer, E. A Deep Chandra ACIS Study of NGC 4151. III. The Line Emission and Spectral Analysis of the Ionization Cone. *Astrophys. J.* **2011**, *742*, 23. <https://doi.org/10.1088/0004-637X/742/1/23>.
88. Ferruit, P.; Wilson, A.S.; Mulchaey, J. Hubble Space Telescope WFPC2 Imaging of a Sample of Early-Type Seyfert Galaxies. *Astrophys. J. Suppl.* **2000**, *128*, 139–169. <https://doi.org/10.1086/313379>.
89. Serafinelli, R.; Marinucci, A.; De Rosa, A.; Bianchi, S.; Middei, R.; Matt, G.; Reeves, J.N.; Braito, V.; Tombesi, F.; Gianolli, V.E.; et al. A remarkably stable accretion disc in the Seyfert galaxy MCG-5-23-16. *Mon. Not. R. Astron. Soc.* **2023**, *526*, 3540–3547. <https://doi.org/10.1093/mnras/stad2801>.
90. Unger, S.W.; Lawrence, A.; Wilson, A.S.; Elvis, M.; Wright, A.E. Radio observations of a hard X-ray selected sample of active galaxies. *Mon. Not. R. Astron. Soc.* **1987**, *228*, 521–531. <https://doi.org/10.1093/mnras/228.3.521>.

Disclaimer/Publisher’s Note: The statements, opinions and data contained in all publications are solely those of the individual author(s) and contributor(s) and not of MDPI and/or the editor(s). MDPI and/or the editor(s) disclaim responsibility for any injury to people or property resulting from any ideas, methods, instructions or products referred to in the content.